PCCP

ROYAL SOCIETY OF CHEMISTRY

PERSPECTIVE

View Article Online
View Journal | View Issue

Cite this: *Phys. Chem. Chem. Phys.*, 2023, **25**, 12668

Research progress and prospects on gas-sensitive mechanisms of semiconductor sensors

Jifeng Chu, Jianbin Pan, Qiongyuan Wang, Aijun Yang,* Shizhen Song, Huan Yuan, Mingzhe Rong and Xiaohua Wang

Received 3rd January 2023,
Accepted 4th April 2023

DOI: 10.1039/d3cp00030c

rsc.li/pccp

Semiconductor materials with wide bandgaps are extensively employed for gas detection due to their advantages of low cost, high sensitivity, fast speed, excellent stability, and distinctive selectivity. Previous studies have reported on different kinds of semiconductor materials and their complex synthesis procedures. However, the research progress on gas-sensitive mechanisms seriously lags behind the performance improvement. The research route of the gas-sensing mechanism is not clear, resulting in an unclear development direction of novel sensitive materials. This review aims to summarize existing approaches and their progress on the interpretation of gas-sensing mechanisms in semiconductors, such as the calculations based on density functional theory, semiconductor physics, and *in situ* experiments. Ultimately, a reasonable route for the mechanism investigation has been proposed. It guides the development direction of novel materials and reduces the cost of screening highly selective materials. Overall, this review can provide helpful guidance concerning the gas-sensitive mechanism for scholars.

1 Introduction

Gas detection is of great significance for industrial production,[1] air-pollution monitoring,[2] healthcare,[3] the Internet of Things (IoT),[4] among others. To achieve accurate analysis of target gases, abundant advanced techniques have been adopted, such as gas chromatography (GC),[5] gas chromatography-mass spectrometry (GCMS),[6] Fourier transform infrared spectroscopy (FTIR),[7] and photoacoustic spectrum (PAS).[8] However, these detection methods rely on precision instruments, which are costly, bulky, and restricted by detection speed. Unlike sophisticated devices, gas sensors are easier to deploy, enabling online monitoring.[9–12]

According to diverse working principles, there are various types of gas sensors, including semiconductor,[13] catalytic combustion,[14] electrochemical,[15] optical,[16] and thermal conductivity.[17] Compared with other sensors, semiconductor sensors have superior advantages of low cost, small size, easy integration, and online monitoring capability. By calculating the variation in the resistance of the material, the concentration of the gaseous analyte can be deduced.[18] The performance indices for evaluating gas sensors mainly include sensitivity, selectivity, stability, and speed. Additionally, the linearity, range, and the limit of detection (LOD) are significant metrics.[19,20] The basic structure of chemical-resistive semiconductor sensors includes sensitive materials and substrates, and the key determinant of the sensor performance is the sensitive material that covers the substrate. By tuning the morphology and microstructure, the performance of the semiconductor sensor can be adjusted.[21] Accordingly, many scholars focused on developing novel semiconductors as gas-sensitive materials, such as TMOs,[13] TMDs,[22] carbons,[23] and organics.[24] Due to the different orientations of micro-morphology, the dimensionality of materials can be roughly divided into 0, 1, 2, and 3.[25] Among them, colloidal quantum dots (QDs) are commonly regarded as 0-dimensional materials.[26] Colloidal quantum dots are solution-synthesized and processed semiconductor nanocrystals with physical dimensions below their Bohr radius.[27] The nanometer scale in three dimensions makes it have an extremely high specific surface area. Moreover, 1-dimensional materials have two dimensions at the nanometer scale,[28] including nanorods, nanowires, nanotubes, and others. Two-dimensional materials have one dimension at the nanometer scale,[29] including nanosheets, and nanofilms. For 3-dimensional materials, they are nanostructured blocks with large size, including nanoparticles, nanocubes, and nanospheres. In addition, the self-assembly of many simple units can generate complex structures. For instance, Jaisutti *et al.*[30] have synthesized a ZnO nanoflower that was assembled from abundant nanosheets. Except for the specific surface area decided by the morphology and microstructure,[31] the vacancy defects,[32] heterojunction[33] and catalysis[34] also influence the performances of gas-sensitive materials, as illustrated in Fig. 1.

Even though numerous studies have attempted to improve the performance of gas sensors, it is difficult to investigate the

---

State Key Laboratory of Electrical Insulation and Power Equipment, Xi'an Jiaotong University, Xi'an 710049, China. E-mail: yangaijun@mail.xjtu.edu.cn

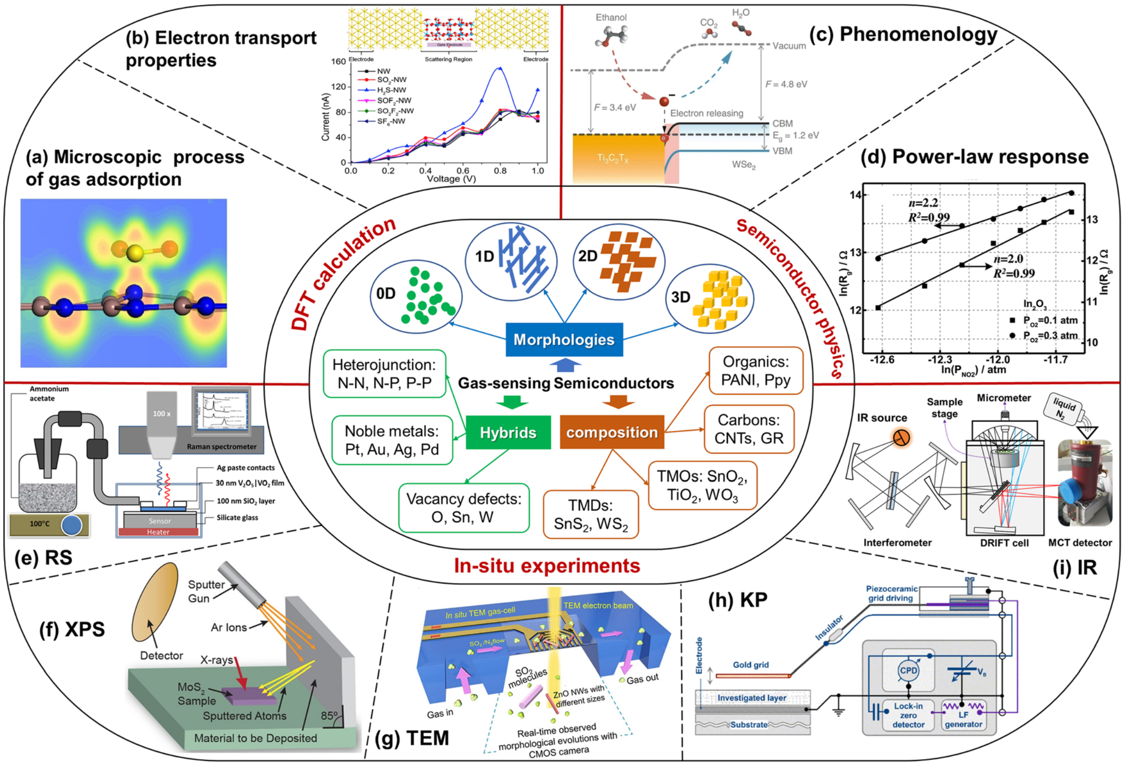

Fig. 1 The proposed methods to study the gas-sensitive mechanisms of semiconductor materials. Specifically, the methods based on DFT calculation contain (a) microscopic process of gas adsorption (reprinted with permission from ref. 40, copyright (2019) Elsevier B.V.), (b) electron transport properties (reprinted with permission from ref. 41, copyright (2020) Elsevier B.V.). The methods based on semiconductor physics contain (c) phenomenology (reprinted with permission from ref. 42, copyright (2020) Springer Nature), (d) power-law response (reprinted with permission from ref. 43, copyright (2018) Elsevier B.V.). The methods based on *in situ* experiments contain (e) RS (reprinted with permission from ref. 44, copyright (2017) IOP Publishing), (f) XPS (reprinted with permission from ref. 45, copyright (2017) American Chemical Society), (g) TEM (reprinted with permission from ref. 46, copyright (2021) American Chemical Society), (h) KP (reprinted with permission from ref. 47, copyright (2009) Elsevier B.V.), (i) IR (reprinted with permission from ref. 48, copyright (2022) Elsevier B.V.).

mechanism underlying the gas-sensing characteristics.[9] In order to screen for ideal semiconductor materials, researchers have to make a great effort on the high-throughput measurement,[35,36] which requires a lot of time and labor costs. In general, if theoretical guidance related to the inner mechanism is lacking, the acquisition of the gas-sensitive material toward the target gas will be full of contingencies. It is hard to develop novel semiconductor materials with superior performance. Therefore, it is of great significance to study the gas-sensitive mechanism behind semiconductor materials. Fig. 1 shows three available routines to reveal the mechanism, including density functional theory (DFT)-based first-principles calculation,[37] semiconductors physics,[38] and *in situ* experiments.[39] Regardless of the types of gas-sensing materials, these methods are universally applicable, but different methods have different superiorities and inferiorities.

Herein, we have briefly summarized the current research progress on the gas-sensitive mechanism of semiconductor materials, and presented many examples to illustrate the differences in various methods. At the end of this review, we also highlight a reasonable route for the investigation of the gas-sensitive mechanism, which may guide the development direction of novel materials and reduce the cost of screening highly selective materials.

2 The approaches to gas-sensing mechanism

Many approaches have been proposed to solve this issue, including the first-principles calculation based on DFT, the physics of semiconductors, the experiments based on *in situ* characterizations. The definition and usage of these methods have been elaborated in this section.

2.1 Computational simulation based on density functional theory

The DFT calculation has been widely used in many fields, including gas sensors,[49] electrochemical batteries,[50,51] biopharmaceuticals,[52–55] optics,[56] and others. The explanation of the mechanism with computational approaches has greatly accelerated the development of functional materials. First-principles calculation is based on DFT. It uses the distribution of space charge to study the properties of polyatomic systems, calculating the electronic structure and intrinsic energy between gas molecules and sensitive materials. Before and after the adsorption of gas molecules, the variations of adsorption energy, charge transfer, density of state (DOS), and work function can be obtained from the DFT calculations.[41,57]

Commercial software is indispensable for the first-principles calculations. Among them, the Vienna *ab initio* simulation package (VASP) is usually employed to accomplish the DFT calculation. The interaction between electrons and ions is performed by the projector augmented-wave (PAW) pseudopotential combined with Perdew–Burke–Ernzerhof (PBE) of the generalized gradient approximation (GGA).[58–60] The method of Grimme-D2 is used to describe the van der Waals (vdW) interactions.[61] The calculation of charge transfer is based on the iterative Hirshfeld (HI) scheme.[62]

2.1.1 Microscopic process of gas adsorption.

Traditional material lattices use periodic boundary conditions, and the established simulation model will expand infinitely in a certain dimension. To some extent, this method can simulate 1D, 2D, and 3D materials, and we can study the adsorption process of various gas molecules on specific crystal surfaces, like (110), (101), (111), and others. However, the dimensions of 0D QDs are between atomic and macroscopic scales,[26] which makes the modeling method of the periodic boundary unsuitable. At this time, it is necessary to set the finite lattice boundary. There have a lot of 0D materials, such as CdSe, SnO_2, and graphene QDs. Fig. 2a and b illustrate the top and side views of BCO_2-graphene QDs.[63] Because of the existence of highly electronegative oxygen atom, graphene tends to attract electrons from the hydrogen molecules. For the effect of carbon atoms on the gas-sensing performance of graphene QDs, Martinez[64] found that the adsorption energy (E_{ad}) between the gas molecule and graphene would gradually decrease with the number of carbon atoms increasing from 6 to 24, and this phenomenon is dominated by the dispersion forces. E_{ad} for the adsorption of H_2O, CO, and NH_3 on Si- and Al-doped graphene can be improved, and it implies that the gas-sensing performance has been enhanced. Similarly, the gas-sensing performances of CdSe and SnO_2 QDs have been investigated by constructing finite models. CdSe QDs as an electron donor has a great interaction with the oxidizing gases (O_2, NO_2).[65] The presence of acidic sites (Sn^{4+} and Sn^{2+}) in SnO_2 QDs makes it attach more NH_3 molecules. The adsorption energy of Sn^{4+} (−1.17 eV) is greater than that of Sn^{2+} (−0.08 eV), which indicates the dominant effect of Sn^{4+} on NH_3 detection.[66] As shown in Fig. 2c, there have been a few investigations concerning the heterojunction of 0D materials, such as CQDs–TiO_2[67] and SnO_2–C_{60},[68] but their potential in gas-sensing remains to be developed.

One-dimensional nanowires are usually modeled in the DFT calculations. The most common are ZnO, WO_3, and CNTs. Among them, ZnO is a well-known functional material with a direct band gap of 3.37 eV, which might have an excellent performance on CO_2 sensing. Srivastava *et al.*[70] constructed a fully relaxed rectangular ZnO nanowire, and found that the CO_2 molecule is physisorbed on the material with a charge transfer of 0.03*e*. During this interaction, the CO_2 molecule transfers the electrons to the nanowire. According to the DOS analysis, this adsorption reaction is due to the van der Waals force, which changes the orbitals of the Zn and O atoms.[71] It should be noted that the practical materials cannot be absolutely perfect, and the surface defects always exist. It is easy to simulate the vacancy defects in materials from the DFT calculation, which can provide a method for studying the impact of defects on the gas-sensitive properties.[72] In Fig. 2d–g, three optimized WO_3 nanowires with an oxygen vacancy (NW-V_a, NW-V_b, NW-V_c) have been employed for NO_2 adsorption.[69] The bottom figures correspond to a single layer of the nanowire with a vacancy. By calculating the adsorption energy (E_{ads}), the adsorption configuration constructed with the N atom orienting to the O_a site of NW-V_b has the lowest value (−3.49 eV), which means that it is the most stable structure.

In Fig. 2h–j, the tunable electronic structures and properties of the WO_3 nanowires lead to a clear change of DOS near the

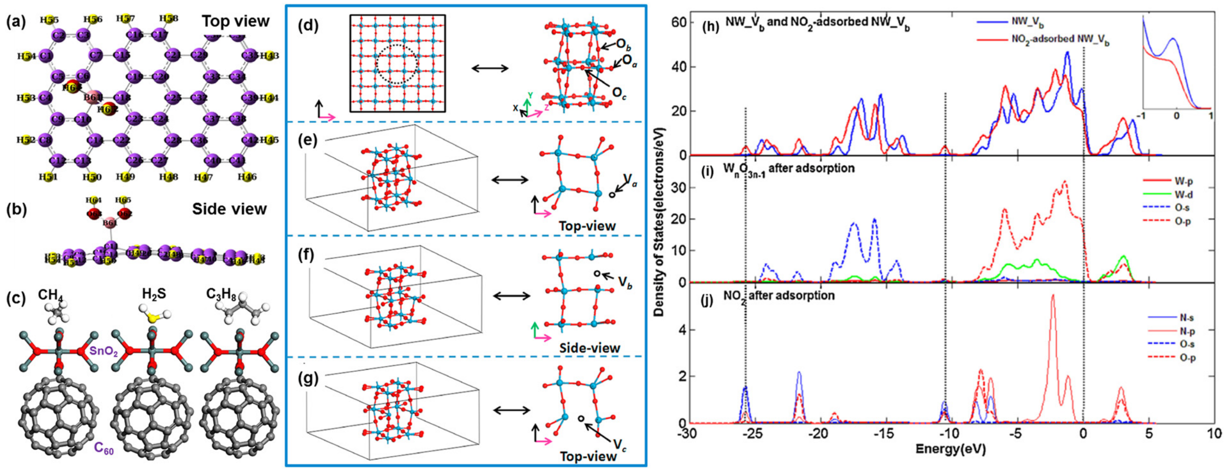

Fig. 2 (a) Top and (b) side views of the optimized BCO_2-graphene QDs. Reprinted with permission from ref. 63, copyright (2022) Elsevier B.V. (c) The schematic of SnO_2–C_{60} QDs towards CH_4, H_2S, and C_3H_8. Reprinted with permission from ref. 68, copyright (2018) Elsevier B.V. (d) The 5 × 5 × 5 WO_3 supercell model for (010)-oriented nanowires. The oxygen-defected WO_3 nanowires of (e) NW-V_a, (f) NW-V_b (g) NW-V_c. (h) Total DOS of the nanowire before and after NO_2 adsorption on the O_a site. PDOS of (i) vacancy-defected WO_3 and (j) NO_2 molecule. The Fermi level is set to zero. Reprinted with permission from ref. 69, copyright (2016) Elsevier B.V.

Fermi level. The charge transfer of the oxygen-defected WO_3 was 4 times more than that of pristine WO_3. According to the results of the Mulliken population analysis,[73,74] the NO_2 molecules prefer to adsorb on the vacancy sites of the WO_3 nanowires because the N atoms are easier to coordinate with the O atoms.[75] The more transferred electrons mean a larger change of conductance. So, the oxygen vacancies have a positive effect on the adsorption of NO_2 molecules on the WO_3 nanowires. Considering that metal-doping is also an effective way to improve the gas-sensitive performance, the carbon nanotubes (CNTs) doped with one Ni atom have been established to react with a mixture of SO_2, SOF_2, and SO_2F_2.[76] These gas molecules tend to absorb near the Ni atom, and greatly change the conductance of CNTs due to the decline of the band gap (E_g). It demonstrates the potential of atomic metal doping to improve the gas-sensitive properties.

Apart from 1D nanowires, a large number of 2D nanosheets are usually constructed to explore the microscopic interactions with gas molecules, such as graphene,[77] MXene,[78] phosphorene,[79] tellurene,[80–82] arsenene,[83,84] antimonene,[85] and others. Among them, the $Ti_3C_2T_x$ MXene is a very popular 2D material that selectively etches the specific atoms from the 3D MAX precursors.[86] Liu *et al.*[78] constructed a two-layer α-$Fe_2O_3/Ti_3C_2T_x$ heterojunction to detect acetone vapor, and studied the mechanism based on the DFT calculation. The composite with the (001) crystal surface has the greatest adsorption energy in comparison with single materials, which means better acetone-sensing performance. The reason behind this phenomenon can be ascribed to the formed heterojunction,[87] which can reduce the reincorporation of the electron–hole and transfer more electrons from acetone to the materials' surface. This effect is important to enhance the gas-sensing performance. Moreover, various sites of gas molecules adsorbed onto the material have a great influence on the DFT calculations.

In Fig. 3a, we have constructed four modes of NO_2 adsorption on the O-saturated MoS_2.[88] Compared with the basal planes, the sites on the edge of the (110) planes are more active because of the larger adsorption energy and greater charge transfer. NO_2 molecules are easier to adsorb on Mo atoms. This suggests that the N-monodentate bonding is more effective than other chemisorption modes. For the preparation of MoS_2 nanosheets, one consideration is to increase the exposure of Mo atoms to enhance the sensitivity towards NO_2. Not only can the DFT calculation be used to study the existing materials, but it can also predict the performances of novel materials that have not been used for gas-sensing. In our previous research, the potential performances of MoSSe[89] and GeP[90,91] monolayer were predicted by the DFT calculation. It was found that they might be sensitive to SF_6 decomposition products. Moreover, the hexagonal InN monolayer is regarded as a promising candidate for SO_2 sensing.[40] After doping a Cu adatom on the InN monolayer, its Fermi-level crossed the conduction band. It is similar to a deep n-type doping, which leads to a great increase of conductance. When the SO_2 molecule adsorbs on the pristine InN, some electronically localized regions of S and N atoms marked in red appeared, which are shown in Fig. 3b and c. The electron localization region around the SO_2 molecule is overlapped with the core electron region of the Cu atom. This means that there is

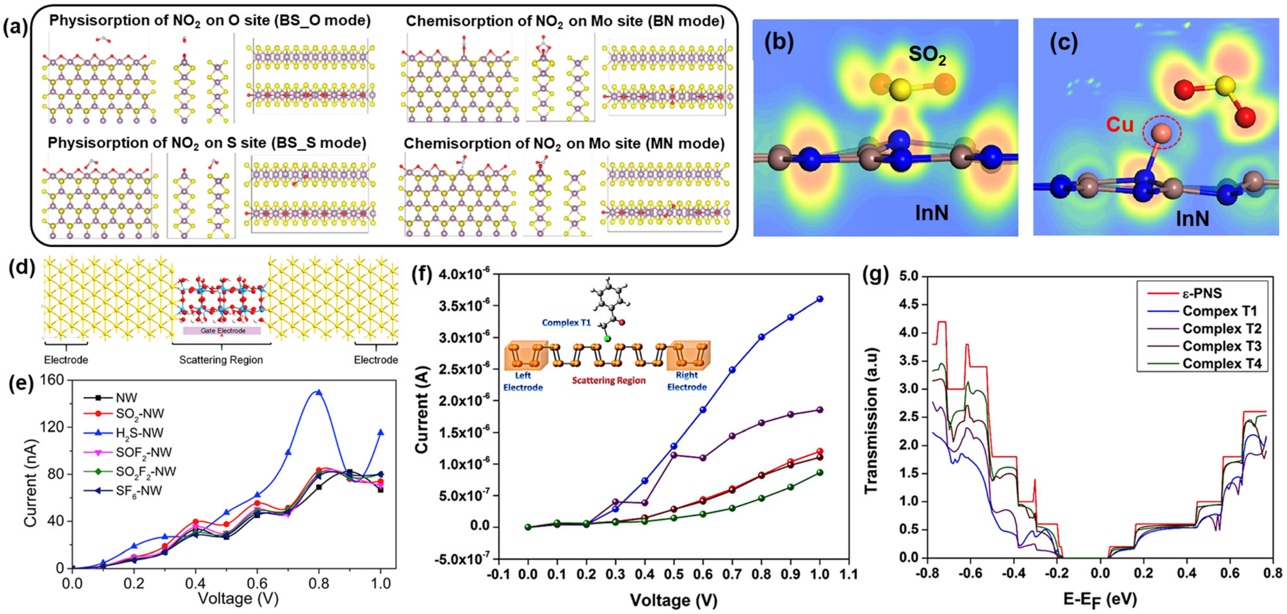

Fig. 3 (a) Side and top views of relaxed O-saturated MoS_2 after the NO_2 adsorption with different modes. Adapted with permission from ref. 88, copyright (2019) John Wiley and Sons. The electron localization function (ELF) of SO_2 molecules adsorbed on (b) the pristine InN and (c) Cu–InN monolayers. Adapted with permission from ref. 40, copyright (2019) Elsevier B.V. (d) The three-probe model in the electron transport properties calculation. (e) Current–voltage curves of perfect WO_3 nanowires with different gas molecules adsorption. Adapted with permission from ref. 41, copyright (2020) Elsevier B.V. (f) *I–V* characteristics of isolated and tear gases adsorbed ε-phosphorene device. (g) Transmission spectrum of the isolated and target gas molecule adsorbed ε-phosphorene device. Adapted with permission from ref. 99, copyright (2020) Elsevier B.V.

an enhanced adsorption effect and strong charge transfer. Thus, metal atom doping can indeed effectively improve the gas-sensing properties of the semiconductor materials.[92,93]

Varying from the 1D and 2D materials, the 3D materials are nanostructured blocks. The DFT calculations only study gas molecules adsorbed on one specific surface, which is cut out of the crystal cell. In our previous research, the adsorption process of various SF_6 decomposed composition products on the (110) surface of SnO_2[94] and CeO_2[57] nanocubes were simulated. The (110) surface is one of the most exposed surfaces of the single crystal, which can best reflect the potential gas-sensitive performances of the nanomaterials. For H_2S and SO_2 molecules adsorbing on the (110) surface of SnO_2, the adsorption energies were larger than that of the other gases. SO_2 had the largest charge transfer, which indicated the strong interaction. The DOS analysis showed that the H_2S adsorption induced an impurity state at the valence band near the Fermi level, which implied a great change in electronic conductivity. On the (110) surface of CeO_2, the calculated adsorption energy follows the order: $SOF_2 > SO_2 > H_2S > SO_2F_2 > SF_6$. The modification of work functions also verified that SF_6 has the slightest interaction. So, the (110) surface of CeO_2 would have excellent selectivity to H_2S, SO_2, and SOF_2 even under the impact of a high-concentration SF_6 environment.

2.1.2 Electron transport property. It is insufficient just to investigate the charge transfer, band structure, and DOS analysis. The electron transport properties give the volt–ampere curves that provide the basis for the gas-sensitive experiments of chemical resistive semiconductors. The electronic transport property can be studied with the nonequilibrium Green's function (NEGF), which is implemented in the Atomistix Toolkit (ATK).[95] The current flowing through the contact region is calculated by the Landauer–Buttiker formula.[96] Based on the NEGF method of DFT calculation, we previously investigated the electronic transport properties of the WO_3 nanowires before and after the adsorption of H_2S molecules.[41] Fig. 3d illustrates the three-stage model, where the resistance change of the WO_3 nanowires is recorded by the current–voltage curves. At an applied voltage of 0.8 V, the current of H_2S–WO_3 is almost twice that of single WO_3, which suggests the significant response towards H_2S. In Fig. 3e, it is worth noting that the current–voltage curve of WO_3 is not monotonous. At some bias voltage points, the current decreases abnormally with the increase of the bias voltages. Also, this anomalous phenomenon was observed in the electronic transport properties of nanowires (SiC and CoO). It can be ascribed to the shift of quasibound states near the Fermi level due to the applied bias voltage.[97,98] This behavior is useful for the fabrication of nanoelectronic devices.

In addition to 1D nanowires, the electronic transport property of 2D nanosheets is often investigated. For instance, Bhuvaneswari *et al.*[99] already verified the potential of ε-phosphorene (PNS) nanosheets to detect tear gas molecules. Fig. 3f shows the *I–V* characteristics of ε-phosphorene for tear gas sensing, and the inset shows the three-stage model. At the voltage of 1 V, the currents of pristine and T1, T2, T3, T4 composites are equal to 1.2, 3.5, 1.8, 1.1, and 0.8 μA, respectively. It suggests that the interactions of 2-chloracetophenone (CAP) on the nanosheets are related to the adsorption structure. Fig. 3g displays a great modification in the transmission when target gas is adsorbed on the ε-PNS. Considering that the transmission spectrum refers to the transmission of electrons from the valence band to the conduction band, the great change in the transmission spectrum implies that there is an amount of transferring charges that influences the sensor resistivity.[100]

Table 1 summarizes the latest results of the DFT calculation for different adsorbed gases. Whether it is 1D, 2D, or 3D

Table 1 The comparisons of DFT calculations for various semiconductor materials

Materials	Morphology	Feature	Target gas	Adsorption energy (eV)	Charge transfer (*e*)	DOS	Transport property	Ref.
CdSe	QDs (0D)	—	NO_2	−0.42	0.415	—	—	65
SnO_2	QDs (0D)	—	NH_3	−1.17	—	—	—	66
Graphene	QDs (0D)	Various atoms	CO	−0.153	—	—	—	101
BCO_2-graphene	QDs (0D)	Atoms doping	H_2	−0.032	—	√	—	63
WO_3	Nanowire (1D)	Oxygen vacancy	NO_2	−3.49	0.84	√	—	69
WO_3	Nanowire (1D)	Oxygen vacancy	SO_2, H_2S	−0.378, −0.388	0.121, 0.137	√	*I–V* curve	41
ZnO	Nanowire (1D)	—	CO_2	−0.48	0.03	√	*I–V* curve	70
CNTs	Nanotube (1D)	Ni doping	SO_2	−1.13	−0.35	√	—	76
GaN	Nanowire (1D)	TiO_2, ZnO, SnO_2 doping	NO_2	−2.31, −1.96, −1.95	—	√	—	102
MoS_2	Nanosheet (2D)	Four active sites	NO_2	−3.73	—	√	*I–V* curve	88
$MoTe_2$	Nanosheet (2D)	—	SO_2	−0.245	−0.086	√	—	103
$Ti_3C_2T_x$–Fe_2O_3	Nanosheet (2D)	Heterojunction	Acetone	−6.70	—	—	—	78
Graphene	Nanosheet (2D)	BN doping	NO_2	−0.221	−0.11	√	—	77
Tellurene	Nanosheet (2D)	α, β phases	NO_2	−0.258, −0.313	−0.173, −0.265	√	—	104
Phosphorene	Nanosheet (2D)	—	SO_2	−0.382	−0.118	√	*I–V* curve	79
ε-Phosphorene	Nanosheet (2D)	T1, T2, T3, T4 structures	Tear gases	−0.502, −0.367, −0.160, −0.101	0.123, 0.054, 0.134, 0.041	√	*I–V* curve	99
BN	Nanosheet (2D)	Al, Si doping	SO_2	−2.224, −1.049	—	√	—	105
InN	Nanosheet (2D)	Cu doping	SO_2, SOF_2, SO_2F_2, HF	−1.38, −0.51, −0.53, −0.78	−0.31, −0.09, −0.33, −0.26	√	—	40
GeP	Nanosheet (2D)	—	NO_2	−0.411	0.338	√	—	90
SnO_2	Nanocube (3D)	(110) surface	SO_2	−0.833	0.084	√	—	94
CeO_2	Nanocube (3D)	(110) surface	H_2S, SO_2, SOF_2	−1.396, −2.292, −2.821	0.360, 0.257, 0.352	√	—	57

material, most focus on the microscopic process of gas adsorption, but rarely study the electronic transport properties. In short, the DFT calculation could acquire the preliminary exploration of the novel materials before the experiments and further raise the screening efficiency. However, the simulation presupposes many assumptions that are far from the actual test conditions. For example, the oxygen vacancy is randomly distributed on the surface of the material, rather than uniformly distributed. The practical size of the doped particles (Au, Pt, *etc.*) on the materials is very large, and thus the simulation of a single atom is not realistic. Furthermore, the influence of the adsorbed oxygen molecules is always neglected, but it is considered to be an important factor in determining the performance.

2.2 Semiconductors physics

Unlike the DFT calculation, gas-sensing experiments provide intuitive methods to evaluate the performance on various target analytes. Typically, the properties of semiconductor sensors are determined by sensitive materials. According to the difference in majority carriers, the semiconductor materials are classified into p-type and n-type, and they perform the opposite properties for reducing and oxidizing gases.

2.2.1 Phenomenology. For the semiconductor sensors, the role of the surface oxygen molecules cannot be ignored. As an electron acceptor, surface oxygen would adsorb on the grains to form the anionic species (like O^{2-}, O^-, and $O_2{}^-$), thereby inducing an electron-depleted layer to increase the surface potential and work function.[100] Fig. 4a and b show the schematic of band bending between grains. The abundant grains between the two electrodes are connected to their neighbors through the boundaries, and it creates a barrier for electron migration on each grain boundary.[18]

When the surface state is lower than the Fermi level, electrons (e^-) will transfer from the conduction band to the surface state until it reaches the equilibrium.

Assuming that the electron density function satisfies the Boltzmann distribution law, the conductance (G), electron density (n_s), and barrier (qV_s) are in accordance with the following equation.

$$G \propto n_s \propto \exp\left(-\frac{qV_s}{kT}\right) \tag{1}$$

where k is the Boltzmann constant, T is the temperature, and q is the basic charge. The height of the barrier determines the material's conductance (G).

When target gas molecules adsorb, a chemical reaction has occurred. It causes the variation of the barrier changes in the conductance, shown as follows.

$$\frac{G_a}{G_g} = \exp\left(\frac{qV_{sg} - qV_{sa}}{kT}\right) = \exp\left(\frac{q\Delta V_s}{kT}\right) \tag{2}$$

where G_a and G_g represent the conductivity of the semiconductor material in air and gas analytes, respectively. qV_{sa} and qV_{sg} are the barriers in air and gaseous analyte, respectively.

Based on the phenomenology of semiconductor physics, eqn (2) can be used to explain the gas-sensing mechanism. Target gas analytes are classified into reducing and oxidizing gases, which lose and gain electrons during chemical reactions, respectively. Taking the n-type semiconductor as an example, the adsorbed anionic oxygen molecules are consumed while reacting with the reducing gases, such as CO and H_2S. The trapped electrons return to the conduction band, causing the barrier height to drop. Accordingly, the resistance of the semiconductor also declined.[106] The larger partial pressure of the reducing gas causes the greater resistance change. Instead, as the electron acceptor, oxidizing gases (like O_2, NO_2) have the opposite effect. An increase in the surface barrier causes an increase in the sensor resistance.[107]

Regardless of the morphology and microstructure of the semiconductor materials, the phenomenological theory is always applicable. In Table 2, we have summarized the previous research using phenomenology to explain the gas-sensitive mechanism. For a 0-dimensional material, Liu *et al.*[108] detected 84 ppb NO_2 at room temperature using PbS quantum dots (QDs). PbS QDs have a strong binding energy towards NO_2, suggesting a competition effect with the adsorbed O_2 molecules. For a 1-dimensional material, Choi *et al.*[109] synthesized the Cr_2O_3-functionalized WO_3 nanorods to detect ethanol. Ethanol might react with the adsorbed oxygen molecules to produce CO_2 and H_2O. The electrons transfer from anionic oxygen to the conduction band of the Cr_2O_3–WO_3 composite. The reduced resistance verified that the composite exhibits the characteristics of the n-type semiconductor. In Fig. 4c and d, a liquid-phase exfoliation technique has been reported to prepare the 2D MXene ($Ti_3C_2T_x$) nanosheets and TMD (WSe_2) nanoflakes,[42] which are very sensitive to ethanol. The $Ti_3C_2T_x$/WSe_2 hybrid shows excellent performance related to the catalytic effect due to the partially occupied band spanning the Fermi level. A chemical reaction occurs between the ethanol molecules and adsorbed oxygen, which releases electrons back into the conduction band and then reducing the resistance.

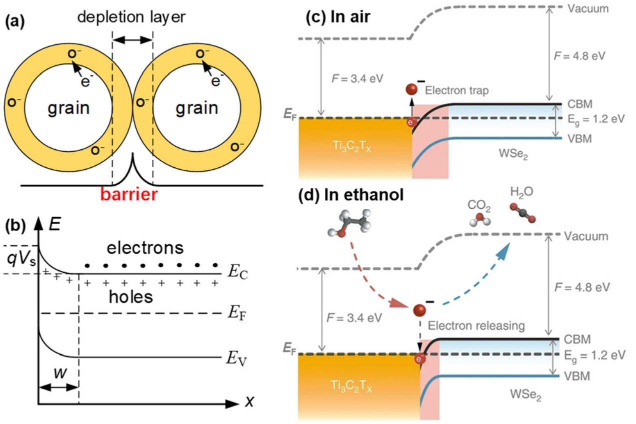

Fig. 4 (a) The illustration of band bending between grains. (b) Surface electron depletion region formed by the adsorbed oxygen. The band of $Ti_3C_2T_x$/WSe_2 in (c) air and (d) ethanol, indicating the variation of the depletion layer with interaction between the adsorbed oxygen and ethanol molecules. Adapted with permission from ref. 42, copyright (2020) Springer Nature.

Table 2 The performance comparisons of various materials based on the semiconductor physics

Material	Feature	Type	Target gas	Concentration (ppm)	Response (R_a/R_g, R_g/R_a)	Electron transfer	Ref.
PdS	Quantum dots (0D)	p	NO_2	50	21.7	Donor	108
ZnO	Quantum dots (0D)	n	H_2S	50	113.5	Acceptor	111
Cr_2O_3–WO_3	Nanorods (1D)	p–n	Ethanol	200	6	Acceptor	109
Pt–ZnO–In_2O_3	Nanowires (1D)	n–n	Acetone	100	55	Acceptor	112
Pd–ZnO–WO_3	Nanofibers (1D)	n–n	Toluene	1	22.22	Acceptor	113
$Ti_3C_2T_x$–SnO_2	Layered structure (2D)	p–n	NH_3	50	1.4	Acceptor	114
$Ti_3C_2T_x$–WSe_2	Nanosheets (2D)	p–n	Ethanol	40	1.092	Acceptor	42
SnO_2–SnS_2	Nanoflakes (2D)	n–n	NO_2	8	5.5	Donor	115
SnO_2–rGO	Nanofilms (2D)	p–n	H_2S	50	33	Acceptor	116
SnO_2–rGO	Nanofilms (2D)	p–n	SOF_2	10	1.032	Donor	117
Co_3O_4	Porous spheres (3D)	n	Ethanol	100	38.2	Acceptor	110

Indeed, the heterojunction is a useful way to improve the sensor performance, and most of the examples in Table 2 have confirmed this point. For the 3D porous Co_3O_4 nanospheres,[110] this phenomenology is still applicable. It should be noted that the morphology improvement like increasing porosity and designing hierarchical structures would only change the sensitivity, not the type of the semiconductor.

2.2.2 Power-law response. Even though phenomenology is intuitive, the interpretation of the gas-sensitive mechanism is very empirical. In order to accurately describe the dependence between the resistance and energy band, scholars are devoted to providing the mathematical formula, namely the power-law response.[43,118] In short, it showed that the sensor resistance is proportional to the partial gas pressure, defined as:

$$R = aP^n \tag{3}$$

where R and P are the resistance of material and the partial pressure of target gas, respectively, and a is the constant. The exponent (n) is a constant related to the gas type.

Table 3 presents some empirical power-laws. However, these exponents lack the theoretical basis.

(1) Reducing target gas. Previous literature has highlighted the role of adsorbed oxygen molecules during the process of chemisorption. The reducing target gas would react with the adsorbed oxygen, and then return the electrons back to the material. At various working temperatures, the adsorption oxygen molecules have different formations on the surface of semiconductor. Assuming that the anionic oxygen exists as O^-, the chemical reaction can be expressed as:

$$O_2 + 2e^- \xleftrightarrow[k_{-1}]{k_1} 2O^- \tag{4}$$

where k_1 and k_{-1} are the rate constants of the forward and backward reactions, respectively, and e^- means the free electron.

The accumulation rate of the O^- species is described as:

$$\frac{d[O^-]}{dt} = k_1 P_{O_2}[e]^2 - k_{-1}[O^-]^2 \tag{5}$$

where the brackets $[\cdot]$ mean the carrier density, and P_{O_2} is the partial pressure of oxygen.

At the equilibrium, the accumulation rate in the left of eqn (5) is equal to zero. So, the surface density of $[O^-]$ can be resolved as:

$$N_t = [O^-] = (k_{O_2}P_{O_2})^{0.5}n_s \tag{6}$$

where k_{O_2} is the equilibrium constant equal to k_1/k_{-1}, and n_s is the density of free electrons.

Due to the difference of adsorbed oxygen, the exponent of the power-law is solved as fractional values of 0.25, 0.5, and 1, corresponding to the charged anionic oxygen (O^{2-}, O^-, and O_2^-) on the surface. Dessimone *et al.*[122] have built three models with various surface reactions. The exponent n changes from 0.25 to 0.5, when the reducing hydrogen exists. It is derived that the oxygen is existed as O^{2-} in the absence of reducing gas, while it adsorbs as O^- in the presence of reducing gas. Furthermore, the presence of water influences the power-law response. Barsan *et al.*[123] provided evidence of SnO_2 porous film for sensing CO. Due to the competition between CO and H_2O for the same anionic adsorbed oxygen, the exponent n significantly declined with the increased concentration of H_2O.

The difference in the width of the electron-depletion region and the bulk size has yielded various exponents of power-law response, as illustrated in Fig. 5a–d.[43,118]

It is clear that the power-law response is size-dependent. When the grain size is far larger than the width of the depletion region, the power-law response is not determined by the semiconductor. When the grain size is close to the depletion region, the power-law would be greatly influenced. To achieve the same exponent n, the surface charge density is increased in the order of sphere, column, and plate. Furthermore, the sensor resistance can be derived as a function of P_{O_2} for the material with spherical and column shapes, and it is also proportional to the ratio of the surface to the volume.

In fact, the exponent n does not strictly follow the power-law response, but has a little error. Fig. 6a shows the power-law response of WO_3, SnO_2, and In_2O_3 to the partial pressure of oxygen (P_{O_2}) in the range from 0.1 to 1 atm. The value of exponent n varies from 0.29 to 0.51, which deviates from the

Table 3 Power-law exponents of the n-type metal oxide semiconductors upon exposure to various gases

Target gas	Material	Exponent	Temp. (°C)	Ref.
O_2	SnO_2	0.5	445	119
CO	SnO_2	−0.5	445	119
NO_2	WO_3	1	200	120
H_2	SnO_2	−0.5	350	121

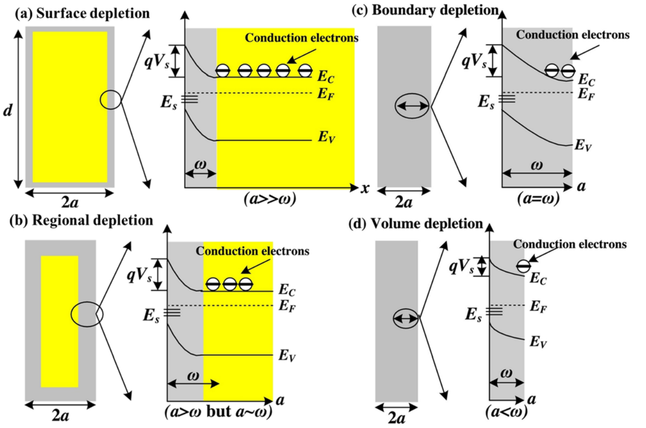

Fig. 5 Electron depletion models of a plate-like grain with various bulk size. (a) Surface depletion model, (b) boundary depletion, (c) regional depletion and (d) volume depletion. Adapted with permission from ref. 43, copyright (2018) Elsevier B.V.

expected fractional values. Owing to the state of surface adsorbed oxygen not being unique, it causes a coexistence of different oxygen molecules and further leads to the deviation in exponent n. For a low concentration of oxygen in the range of 0–1000 ppm, the calibration curves of $\ln R$ *versus* $\ln P_{O_2}$ becomes nonlinear, as shown in Fig. 6b. It can be ascribed to the weakly depleted region because of the decrease of oxygen molecules. At this time, the power-law response should be firstly dominated by n_s and in turn of P_{O_2}.

(2) Oxidizing target gas. As an oxidizing target gas, it is assumed that NO_2 is directly absorbed on the material's surface by the following equation.

$$NO_2 + e^- \underset{k_{-11}}{\overset{k_{11}}{\longleftrightarrow}} NO_2^- \quad (7)$$

According to the law of mass action, the surface density at which NO_2^- reaches the equilibrium can be expressed as:

$$[NO_2^-] = (k_{NO_2} P_{NO_2}) n_s \quad (8)$$

where P_{NO_2} is the concentration of NO2, and k_{NO_2} is the equilibrium constant equal to k_{11}/k_{-11}.

Assuming that P_{O_2} is a constant, the density of NO_2^- is proportional to the density of the electron. In Fig. 6c, the In_2O_3 sensor performs an obvious power-law response towards NO_2 at the constant partial pressures of oxygen (P_{O_2}) of 0.1 and 0.3 atm, respectively. Notably, the effect on the difference in P_{O_2} is very little.

Based on eqn (9) and (10), Maeng *et al.*[124] assumed that the NO_2 molecule consumed the adsorption sites to form NO_2^-. After all the sites are consumed, the excess NO_2 forms NO_2^- on the surface of SnO_2 nanoribbons, expressed as the following two reactions.

$$NO_2^{gas} + \alpha_1 e^- + S_A \leftrightarrow NO_2^{-\alpha_1}(S_A) \quad (9)$$

$$NO_2^{gas} + \alpha_2 e^- + NO_2^{-\alpha_1}(S_A) \leftrightarrow NO_3^{-(\alpha_1+\alpha_2)}(S_A) + NO^{gas} \quad (10)$$

where α_1 and α_2 are the numbers of charge transfer in various reaction processes, and α is equal to the sum of α_1 and α_2. S_A is the adsorption site on the surface. Anionic NO_2^- and NO_3^- are the species generated from NO_2.

The relationship between the sensor response and the concentration of NO_2 can be described as:

$$S = K_{NO_2} C_{NO_2}^{2/(1+\alpha)} \quad (11)$$

At low concentrations of NO_2, the sensor response is dominated by the adsorption of NO_2 molecules on available sites. The process of capturing β electrons from the surface of the semiconductor can be described as:

$$NO_2^{gas} + \beta e^- + S_A \leftrightarrow NO_2^{-\beta}(S_A) \quad (12)$$

The curve of the sensor response *versus* the NO_2 concentration can be defined as:

$$S = K_{NO_2} C_{NO_2}^{1/(1+\beta)} \quad (13)$$

Given that the parameters α and β are less than 1, the exponent equal to 0.69 can only be ascribed to eqn (13). It is clear that the gas-sensing process is dominated by the adsorption of a single NO_2 molecule rather than the formation of the NO_3^- species.

With the power-law response, the parametric description of chemical reactions on the surface of the semiconductor can be

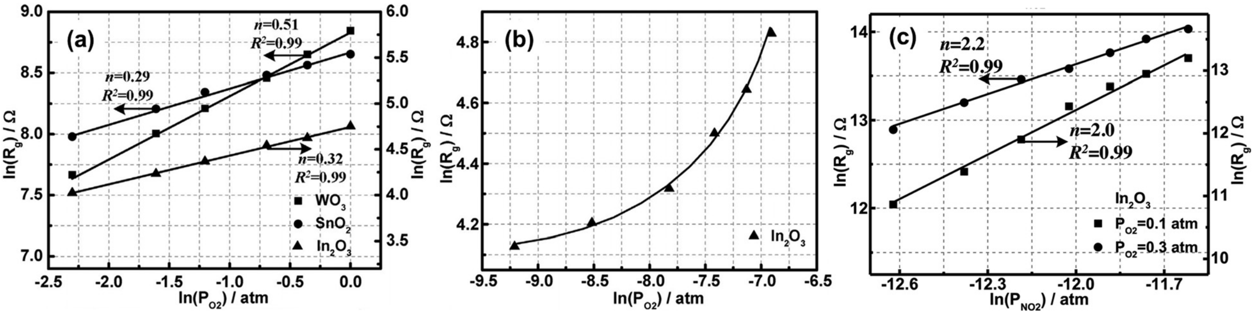

Fig. 6 The power-law response of (a) WO_3, SnO_2, and In_2O_3 to oxygen in the range of P_{O_2} from 0.1 to 1 atm. (b) In_2O_3 to oxygen in the range of P_{O_2} from 0 to 1000 ppm. Adapted with permission from ref. 118, copyright (2018) Elsevier B.V. (c) In_2O_3 to NO_2 in the presence of oxygen at 0.1 and 0.3 atm. Adapted with permission from ref. 43, copyright (2018) Elsevier B.V.

obtained. The exponent reflects the strength of the chemical reaction, related to the state of electron depletion region based on the physics of semiconductors. However, this method only captures the initial and final states after the material adsorbs gas molecules. The intermediate process of the chemical reaction is still unpredictable. Furthermore, the mechanism interpretation by the power-law is very dependent on the anionic adsorbed oxygen, and relevant studies in anaerobic environments are lacking.

2.3 *In situ* experiments

Advanced characterization techniques can reveal the essence of semiconductor materials, containing Raman spectroscopy (RS), X-ray photoelectron spectroscopy (XPS), transmission electron microscope (TEM), Kelvin probe (KP), diffuse reflection infrared Fourier transform spectroscopy (DRIFT), *etc.* However, most approaches only analyze the materials' properties, and it is difficult to monitor the specific adsorption process of gas molecules. A series of *in situ* experiments with precision instruments makes it possible to explore the actual physical and chemical reactions, which is beneficial to explain the mechanism of the semiconductor materials.

2.3.1 Raman spectroscopy. RS is a reliable, sensitive, and nondestructive method that employs the scattering spectroscopy to analyze the structure information of materials based on molecular vibration and rotation.[125] The adsorption of various gas molecules produces various changes in molecular variation, enabling the selectivity for specific gases. Fig. 7a illustrates the RS of SnS_2 nanosheets when exposed to NO_2.[126] After NO_2 injection, there is no obvious Raman peak shift. This means that no chemical bonds are formed during the physical adsorption of NO_2 molecules. In terms of the intensity ratio, the peak intensity of A_{1g} is significantly reduced, whereas E_g seems to be maintained. A_{1g}/E_g decreased from 1.05 to 0.8. It can be assumed that the NO_2 molecules adsorbed on the surface acted as electron acceptors, changing the molecular vibration of SnS_2.

In addition to the intensity variation, the frequency shifts of the RS peaks related to the elastic constant of the material imply the formation of chemical bonds. The blue and red shifts correspond to the acceptance and donation of electrons from gas molecules, respectively. Dunst *et al.*[127] have found that the intensity of the PEDOT band at 1559 cm^{-1} increases with the NO_2 exposure, and the frequency shifts from 1559 cm^{-1} to 1565 cm^{-1} due to the free electrons trapped by NO_2 molecules. Fig. 7b shows the *in situ* Raman spectra of V_2O_5 for sensing NH_3 at 100 °C.[44] It can be observed that the peak at 194 cm^{-1} remains un-shifted, while the 996 cm^{-1} phonon is red-shifted upon the interaction with the NH_3 molecule. Fig. 7c gives the magnified image of 996 cm^{-1} Raman lines. With the injection of NH_3, the Raman line shows a red shift, which indicates that the electrons are transferred from the gas molecules to the adsorbent. Moreover, the increased intensity can be attributed to the adsorption effects, which is related to the phonon confinement model. The stronger adsorption effect brings more Raman scattered photons, and it causes a greater change in intensity.

2.3.2 X-ray photoelectron spectroscopy. XPS can measure the inner electron binding energy. It provides the elemental composition of the adsorbed species, which is used for the surface and interface analysis. Using XPS, it is possible to find electrons captured from chemical bonds.[128] *In situ* experiments can be completed by combining the XPS device with the gas phase system. Fig. 8 shows the selective NO_x adsorption on the oxygenated graphene films.[129]

Upon exposure to NO_2, there has been no significant change in the C 1s spectrum of the material. However, the N 1s spectrum at 404.5 eV increased greatly. A weak interaction between the NO_x molecules and GO and OFG materials has been observed, but the noise makes the spectral intensity hard to distinguish. Given the short mean free path of electrons in the gas phase, the conventional XPS instrument must be limited to the ultrahigh vacuum (UHV). Furthermore, Yamamoto *et al.*[130] studied the adsorption of H_2O on the surface of TiO_2 using *in situ* XPS coupled with a third-generation synchrotron radiation source. At the pressure above 5 torr, the *in situ* XPS proved the formation of a hydroxyl groups first, followed by molecular water adsorption.

2.3.3 Transmission electron microscope. TEM can observe the morphology and microstructure of the materials. TEM used the highly focused ultra-fine electron beam to scan the sample's surface. The secondary electrons related to the incident angle are excited, and the surface microstructure of the sample is calculated by the incident angle. After a series of amplification processing,

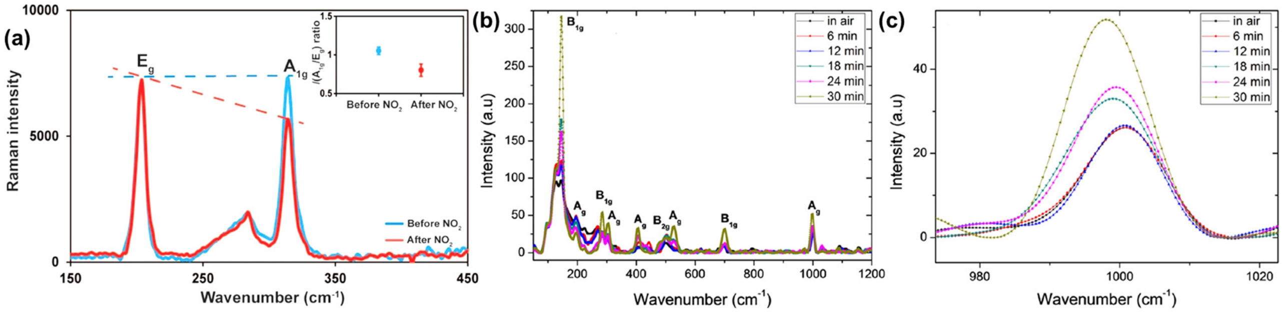

Fig. 7 (a) Raman spectra of SnS_2 flakes before and after NO_2 exposure. Adapted with permission from ref. 126, copyright (2015) American Chemical Society. (b) Raman spectra at 100 °C of V_2O_5 upon exposure to NH_3 recorded at 6 min intervals. (c) Magnified image of 996 cm^{-1} Raman lines. Adapted with permission from ref. 44, copyright (2017) IOP Publishing.

the morphology is determined by the second electronic signal. A TEM equipped with an energy dispersive spectrometer (EDS) can analyze the elemental composition of the sample.[131] With the development of ambient TEM, it has been demonstrated that the dynamic morphology change can be captured in solid or gas phases, even at the solid–liquid interface. Using MEMS technique, Wang *et al.*[46] fabricated a gas cell for real-time observation of the microscopic morphology of ZnO nanowires in the reaction with SO_2 (1 bar).

In Fig. 9a–h, the shell thickness around the ZnO nanowire increases correspondingly with the reaction time. Meanwhile, the core of the ZnO nanowire gradually became thinner. It is shown that ZnO on the surface of the nanowire is transformed into $ZnSO_3$. Fig. 9i presents the results of EDS mapping, which prove that the S element exists within the shell, but the Zn element mainly exists in the core of the nanowire. In their other research, the *in situ* TEM technique was used to investigate the deactivation mechanism of bimetallic Pd–Ag nanoparticles after adsorbing H_2.[132] At the temperature of 300 °C, both types of nanoparticles bind to neighboring nanoparticles. The decline in the gas contact area leads to the decrease in the catalytic capability. When the temperature is further increased to 500 °C, Ag migrates from the bimetallic alloy, weakening the synergistic effect on H_2 catalysis.

2.3.4 Kelvin probe. The Kelvin probe is a non-contact measurement technique consisting of a reference electrode and a sample electrode. Both electrodes create a parallel capacitor whose value varies with the spacing of the two electrodes.[133] The illustration is presented in the set of Fig. 10. The contact potential differences (CPD) is determined as:

$$I(t) = g_{\mathrm{KP}}u(t) = g_{\mathrm{KP}}[\mathrm{CPD}(t) - V_{\mathrm{B}}(t)] \tag{14}$$

The intercept with the abscissa corresponds to the zeroing condition of the locking method, shown as follows,

$$\begin{cases} I(t) \equiv 0 \\ \mathrm{CPD}(t) = V_{\mathrm{B}}(t) \end{cases} \tag{15}$$

where g_{KP} is a parameter named the KP conductance.

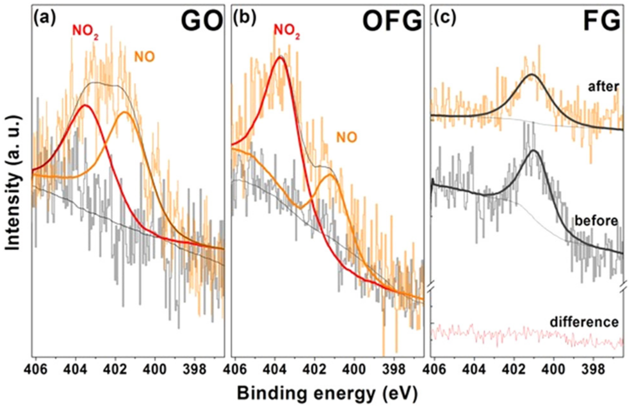

Fig. 8 XPS N 1s spectra of (a) GO, (b) OFG, (c) FG films before (gray line) and after (orange line) the NO_x gas adsorption. Adapted with permission from ref. 129, copyright (2018) John Wiley and Sons.

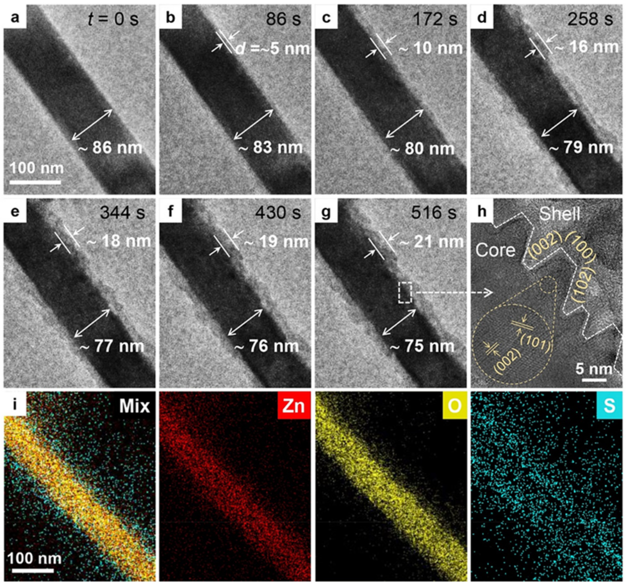

Fig. 9 (a)–(g) Morphological images of a single ZnO nanowire under an atmosphere of SO_2. (h) The high-resolution image of the zigzag interface after the adsorption reaction. (i) EDS mapping of the ZnO nanowire that was completely reacted with SO_2 molecules. Adapted with permission from ref. 46, copyright (2021) American Chemical Society.

Fig. 10 proves that the current amplitude is equal to zero when the backing potential (V_B) is equal to CPD. Otherwise, the sinusoidal current exists in both electrodes.[47] When gas molecules adsorb on the material, the work function and surface potential of the material change. Therefore, *in situ* KP is usually used to study the gas-sensitive mechanism. Pearce *et al.*[134] demonstrated that monolayer graphene had a larger shift in surface potential than double-layer graphene upon exposure to NO_2.

Fig. 11a and b present the surface potential in the areas and extracted line profiles, respectively. Notably, the difference in the surface potential between 1LG and 2LG is very small (<5 mV). With the injection of NO_2, the difference in the surface potential gradually increases to 25 mV. Fig. 11c shows the surface potential when exposed to NO_2. The lines with different colors

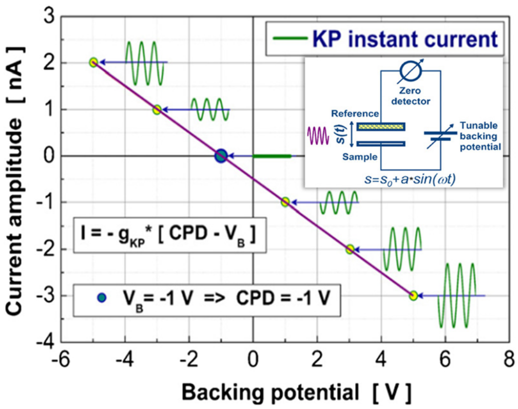

Fig. 10 The dependency of the KP current on the applied backing voltage for a pair of electrodes. Adapted with permission from ref. 47, copyright (2009) Elsevier B.V.

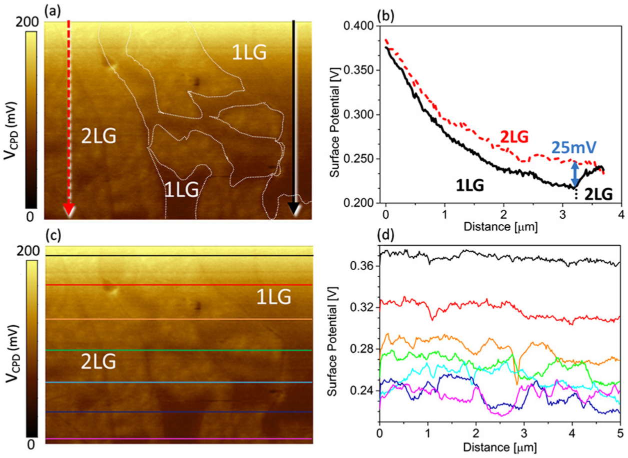

Fig. 11 (a) The decreased surface potential map with NO_2 exposure. (b) The surface potential of 1LG and 2LG in the extracted line profile. (c) The surface potential map shows extracted line profile sites. (d) The extracted line profiles show the decreasing surface potential with the increase of NO_2 exposure time. Adapted with permission from ref. 134, copyright (2013) American Chemical Society.

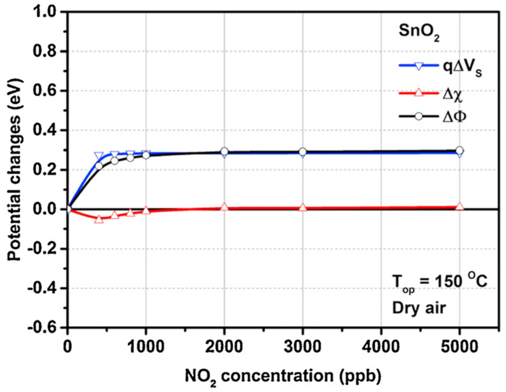

Fig. 12 The effect of NO_2 exposure under a dry background over the potential changes of SnO_2 sensitive material. Adapted with permission from ref. 136, copyright (2016) Elsevier B.V.

represent different extracted profiles, which are plotted in Fig. 11d. The drop rate of the surface potential is initially fast, but gradually slows down. It means that the material has reached a stable state of adsorption saturation with the increase of NO_2 exposure time.

Based on the simultaneous measurements of resistance and work function, the changes in electronic affinity ($\Delta\chi$) can be calculated as:

$$\Delta\chi = \Delta\phi - kT\ln S = \Delta\phi - q\Delta V_s \tag{16}$$

where k is the Boltzmann constant and T is the temperature. The sensor response (S) is defined as R_g/R_a. $\Delta\phi$ and ΔV_s are the changes of work function and surface potential, respectively.

Assuming that the electron affinity remains constant throughout the entire process and the interaction of gas adsorption is limited to the surface of the material, the change in CPD after gas exposure is only related to the change in work function.

$$\Delta \mathrm{CPD} = -\Delta\phi = -e\Delta V_s \tag{17}$$

Considering that the conductance of single-crystalline films is related to the surface electrostatic potential, Simion *et al.*[135] have used the *in situ* KP to record the variations of work function by measuring the changes in the contact potential difference (CPD) between the sample and the reference electrodes. They have demonstrated the dependence of sample conductance on band bending. The surface potential equal to zero means a flat band that the material has transformed from the electron-depleted state to the electron-accumulated state. In Fig. 12, Stanoiu *et al.*[136] used eqn (16) to explain the essence of NO_2 adsorption. In air, the qV_s values above 0.200 eV leads to a fully depleted state, which is equivalent to the concentration of NO_2 being higher than 400 ppb.

2.3.5 Diffuse reflection infrared Fourier transform spectroscopy.

For the above *in situ* experimental methods, XPS and TEM are very expensive, and can only work in the condition of high vacuum. KP shows a variation of the surface potential, but does not have the ability to identify various gases. Although the *in situ* RS is easy to implement, the adsorption of gas molecules has little effect on the vibration modes of the material, and it is difficult to observe the obvious variations in frequency shift and peak intensity. The Fourier transform infrared absorption spectrum has several modes, including transmittance (TR),[137] attenuated total reflection (ATR),[138] and diffuse reflection (DR).[139] The species formed on the material's surface can be identified by analyzing the position, intensity, and shape of the absorbance bands. After exposure to various gases, *in situ* diffuse reflection infrared Fourier transform (DRIFT) spectroscopy can explore the functional groups and mediate species on the material's surface, and the chemical reaction pathways can be further derived. In addition, the mercury cadmium telluride (MCT) detector is commonly used to acquire the high resolution.

Kim *et al.*[140] reported the effect of doping with different proportions of NiO on the humidity sensitivity of SnO_2. According to the *in situ* DRIFTs, H_2O molecules were mainly adsorbed on NiO, whereas no interaction between H_2O and SnO_2 was observed. It was proved that SnO_2 doped with NiO could perform the same gas-sensing performance, and decline the humidity dependence without the sensitivity loss.

For complex gas molecules, *in situ* DRIFT still shows the adsorption process. Zhang *et al.*[143] employed SnO_2 nanoparticles to detect TCE. A series of characteristic bands can be observed during the interaction. According to the vibration mode of the chemical bonds, the probable species on the SnO_2 can be attributed to DCAC, phosgene, $CHCl_3$, HCl, CO_2, CO, H_2O, and Cl_2. Likewise, Song *et al.*[144] studied the adsorption mechanism of diethyl ether by *in situ* DRIFTs. During the interaction of diethyl ether with the SnO_2/rGO film, the bands of CH_3CH_2OH, HCHO, CH_3CHO, C_2H_4, H_2O, and CO_2 were found. The working temperature has a great influence on the performance of gas-sensitive material, varying the gas adsorption–desorption spectra of the material.

Under the adsorption of SO_2, *in situ* DRIFTs of CeO_2 at 300, 350, and 450 °C are shown in Fig. 13a.[141] The band at 1180 cm^{-1} is assigned to bulk-like sulfates in CeO_2. The formed metal

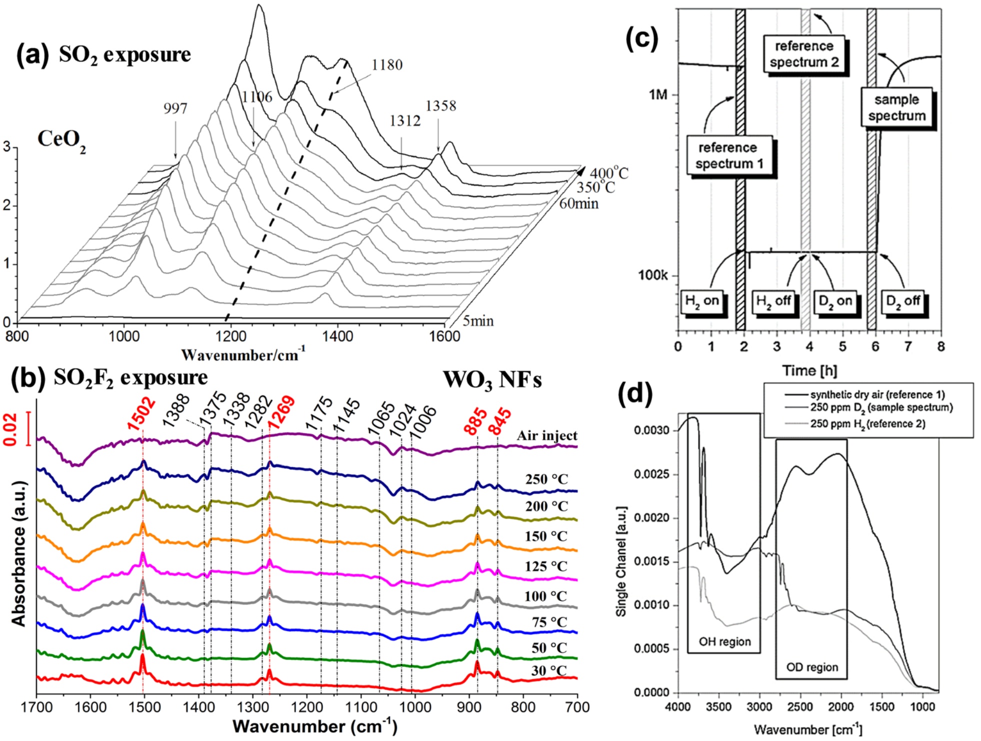

Fig. 13 (a) *In situ* DRIFTs SO_2 adsorption spectra over CeO_2 at 300 °C for 60 min, 350 and 450 °C for 10 min. Adapted with permission from ref. 141, copyright (2015) Elsevier B.V. (b) *In situ* DRIFTs of ZIF8-WO_3 after SO_2F_2 adsorption with the temperature variation. Adapted with permission from ref. 48, copyright (2022) Elsevier B.V. The operando for the variations of (c) DRIFTs and (d) resistance of SnO_2 under exposure of 30 ppm H_2. Shadows regions mean the DRIFTs are tested at air and 10 ppm H_2. Adapted with permission from ref. 142, copyright (2012) Elsevier B.V.

sulfates block the active sites, which is responsible for the irreversible deactivation of materials. Considering that various morphologies also affect the performance, Luo *et al.*[145] have compared the *in situ* DRIFTs of ZnO nanowires and nanoplates upon exposure to SO_2. Compared with ZnO nanowires, ZnO nanoplates absorbing SO_2 do not show any evident features. So, the micro-morphology indeed decides the properties of the gas-sensitive materials. In addition, we have explored the adsorption of SO_2F_2 on WO_3 nanowires by *in situ* DRIFTs.[48] In Fig. 13b, 1502 and 1269 cm^{-1} are attributed to the symmetric and antisymmetric stretching vibration of the O=S=O bond, respectively. The peaks at 885 and 845 cm^{-1} are assigned to the symmetric and anti-symmetric stretching vibrations of the F–S–F bond, respectively. With the temperature increasing, the intensities

Table 4 The comparisons of various *in situ* experiments for the mechanism explanation

Method	Material	Feature	Target gas	Observation	Ref.
RS	V_2O_5	Nanoparticles	NH_3	Peak intensity, frequency shift	44
RS	SnS_2	Nanoflakes	NO_2	Peak intensity	126
RS	PEDOT–rGO	Nanofilms	NO_2	Peak intensity, frequency shift	127
RS	MWCNT	Nanotubes	NH_3	Peak intensity	146
XPS	TiO_2	(110) crystal face	H_2O	Peak intensity	130
XPS	Pd	(100) crystal face	CO	Peak intensity	147
XPS	GO, OFG, FG	Nanofilms	NO_2, NO	Peak intensity	129
TEM	ZnO	Nanowires	SO_2	Morphological image, EDS mapping	46
TEM	Cu–Au	Single-crystal films	H_2	Morphological image	148
TEM	Pd–Ag	Nanoparticles	H_2	Morphological image	132
KP	Graphene	Nanolayers	NO_2	Surface potential	134
KP	SnO_2	Porous nanoparticles	NO_2	Surface potential	136
KP	SnO_2	Nanoparticles	H_2, CO, O_2, NO_2	Surface potential	135
DRIFTs	NiO–SnO_2	Hierarchical spheres	CO	Band position and intensity	140
DRIFTs	SnO_2	Nanofilms	Trichloroethylene	Band position and intensity	143
DRIFTs	ZnO	Nanowires and nanoplates	SO_2	Band position and intensity	145
DRIFTs	SnO_2–rGO	Nanofilms	Diethylether	Band position and intensity	144
DRIFTs	MOF–WO_3	Nanowires	H_2S, SO_2, SOF_2, SO_2F_2	Band position and intensity	48
Operando	SnO_2	Nanoparticles	CO, H_2	Band position and intensity, sensor response	142
Operando	SnO_2	Nanoparticles	H_2	Band position and intensity, sensor response	149

of the bands at 1502 and 1269 cm^{-1} gradually decreased, which means that the desorption of SO_2F_2 from the surface of the nanofibers is accelerated.

In recent years, the notion of *operando* has received extensive attention to improve the DRIFTs. It not only records the spectra, but also tests the sensor resistance. After exposure to hydrogen, Fig. 13c shows the resistance of SnO_2 as a function of the marking time interval, in which the reference spectra and sample spectrum were recorded.[142] Fig. 13d displays the corresponding single-channel DRIFT spectra. With the injection of H_2, the OH groups are distributed in the range of 3000–3900 cm^{-1}. It demonstrates the chemical reaction of H_2 with adsorbed oxygen to form H_2O. At the same time, the reduced sensor resistance means the charge transfer. In Table 4, we have summarized current *in situ* experiments to elucidate the mechanism of semiconductor materials.

3 Summary and outlook

The semiconductor gas sensors have been widely employed in environmental monitoring, industrial manufacturing, and the internet of things. The key to deciding the sensitive performance is the semiconductor material. Although the novel materials are emerging in an endless stream, the gas-sensing mechanisms are far lagging. It is of great significance that the mechanism investigation can provide the developing directions for novel materials. Herein, we have summarized a series of approaches to study gas-sensitive mechanisms, including the DFT calculation, phenomenology, power-law response, and *in situ* characterization. Different methods have different superiority and inferiority. The DFT calculation can simulate the adsorption process of gas molecules on the materials, applicable for rapid selection. Whereas, this method makes many assumptions in advance, which makes the simulation far from experiment. More importantly, the anionic adsorbed oxygen plays an important role in the interaction with the materials, but it cannot be simulated. The semiconductor physics connects the sensor resistance with the barrier, and the variation in resistance means the change of absorbed oxygen molecules on the semiconductor materials. The power-law response provides the parametric description of the phenomenology. Although the reaction occurring on the grain can be ascribed to the content of adsorbed oxygen, the intermediate process is not available. With the precision instruments, *in situ* experiments can infer the reaction pathways of gas molecules with semiconductor materials, and further reveal the mechanism.

Based on the mechanism explanation, a reasonable procedure of developing novel materials is proposed as follows. (1) Use the DFT calculations to scope the range of potential gases. (2) Deduce the probable reaction between the gas molecule and sensitive material by power-law response. (3) Analyze the essence of material degradation by *in situ* tests, and guide the optimization direction of novel materials.

Overall, the gas-sensitive mechanism of semiconductor materials is facing many challenges and opportunities. Some distinct possibilities could spearhead the relevant research. (1) The DFT calculation is usually employed to study the effects of atom vacancy and atom doping, but there are very few heterojunctions. (2) Each method has its boundaries, and it is useful to integrate multiple *in situ* methods to explore the process of gas adsorption from various perspectives. (3) Novel techniques and precision instruments might attract the interest of a wide community.

Author contributions

All authors contributed to this manuscript.

Conflicts of interest

There are no conflicts of interest to declare.

Acknowledgements

This work was supported by the National Natural Science Foundation of China (No. U2166214 and No. 52207170), Shaanxi Province ''Sanqin scholars'' Innovation Team Project (Demonstration innovation team of Xi'an Jiaotong University for the key technology of advanced DC power equipment and its industrialization), China Postdoctoral Science Foundation (No. 2022M712510 and 2022TQ0252), Natural Science Basic Research Program of Shaanxi (Program No. 2023-JC-JQ-41), Key Research and Development Program of Shaanxi (Program No. 2022GXLH-01-11 and N2022GY-273), State Key Laboratory of Electrical Insulation and Power Equipment (No. EIPE23314 and No. EIPE23408), K. C. Wong Education Foundation, the Fundamental Research Funds for the Central Universities.

References

1 T. Seiyama, A. Kato, K. Fujiishi and M. Nagatani, *Anal. Chem.*, 1962, **34**, 1502–1503.
2 J. Chu, W. Li, X. Yang, Y. Wu, D. Wang, A. Yang, H. Yuan, X. Wang, Y. Li and M. Rong, *Sens. Actuators, B*, 2021, **329**, 129090.
3 N. Kumar, N. P. Shetti, S. Jagannath and T. M. Aminabhavi, *Chem. Eng. J.*, 2022, **430**, 132966.
4 D. Wang, J. Pan, X. Huang, J. Chu, H. Yuan, A. Yang, N. Koratkar, X. Wang and M. Rong, *IEEE Int. Things J.*, 2022, **9**, 5502–5510.
5 H. E. Tahir, Z. Xiaobo, H. Xiaowei, S. Jiyong and A. A. Mariod, *Food Chem.*, 2016, **206**, 37–43.
6 O. Koreh, T. Rikker, G. Molnar, B. M. Mahara, K. Torkos and J. Borossay, *Rapid Commun. Mass Spectrom.*, 1997, **11**, 1643–1648.
7 J. Gao, Y. Zhang, X. Li, G. Shi and Y. Zhang, *IEEE Trans. Instrum. Meas.*, 2022, **71**, 1–8.
8 J. P. Waclawek, R. Lewicki, H. Moser, M. Brandstetter, F. K. Tittel and B. Lendl, *Appl. Phys. B*, 2014, **117**, 113–120.
9 H. Ji, W. Zeng and Y. Li, *Nanoscale*, 2019, **11**, 22664–22684.

10 I. Fratoddi, I. Venditti, C. Cametti and M. V. Russo, *Sens. Actuators, B*, 2015, **220**, 534–548.

11 J. Chu, Q. Wang, Y. Liu, J. Pan, H. Yuan, A. Yang, X. Wang and M. Rong, *IEEE Trans. Power Delivery*, 2022, 1–9.

12 J. Chu, A. Yang, Q. Wang, X. Yang, D. Wang, X. Wang, H. Yuan and M. Rong, *Microsyst. Nanoeng.*, 2021, **7**, 1–18.

13 E. Comini, *Anal. Chim. Acta*, 2006, **568**, 28–40.

14 A. Hosoya, S. Tamura and N. Imanaka, *ISIJ Int.*, 2016, **56**, 1634–1637.

15 E. Bakker and M. Telting-Diaz, *Anal. Chem.*, 2002, **74**, 2781–2800.

16 H. Kim, S. Z. Uddin, D. Lien, M. Yeh, N. S. Azar, S. Balendhran, T. Kim, N. Gupta, Y. Rho, C. P. Grigoropoulos, K. B. Crozier and A. Javey, *Nature*, 2021, **596**, 232–237.

17 W. Cho, T. Kim and H. Shin, *Sens. Actuators, B*, 2022, **371**, 132541.

18 N. Yamazoe and K. Shimanoe, *Sens. Actuators, B*, 2008, **128**, 566–573.

19 A. Hierlemann and R. Gutierrez-Osuna, *Chem. Rev.*, 2008, **108**, 563–613.

20 S. J. Kim, H. Koh, C. E. Ren, O. Kwon, K. Maleski, S. Cho, B. Anasori, C. Kim, Y. Choi, J. Kim, Y. Gogotsi and H. Jung, *ACS Nano*, 2018, **12**, 986–993.

21 N. Yamazoe, *Sens. Actuators, B*, 1991, **5**, 7–19.

22 X. Duan, C. Wang, A. Pan, R. Yu and X. Duan, *Chem. Soc. Rev.*, 2015, **44**, 8859–8876.

23 S. Cui, S. Mao, G. Lu and J. Chen, *J. Phys. Chem. Lett.*, 2013, **4**, 2441–2454.

24 L. Wang, H. Huang, S. Xiao, D. Cai, Y. Liu, B. Liu, D. Wang, C. Wang, H. Li, Y. Wang, Q. Li and T. Wang, *ACS Appl. Mater. Interfaces*, 2014, **6**, 14131–14140.

25 J. Lee, *Sens. Actuators, B*, 2009, **140**, 319–336.

26 Z. Song, J. Liu, Q. Liu, H. Yu, W. Zhang, Y. Wang, Z. Huang, J. Zang and H. Liu, *Sens. Actuators, B*, 2017, **249**, 632–638.

27 Y. Shirasaki, G. J. Supran, M. G. Bawendi and V. Bulović, *Nat. Photonics*, 2013, **7**, 13–23.

28 W. Oum, A. Mirzaei, T. Hussain, J. H. Bang, S. Han, K. Y. Shin, D. J. Yu, S. Kang, T. Kaewmaraya, S. S. Kim and H. W. Kim, *Sens. Actuators, B*, 2022, **363**, 131853.

29 S. Yang, C. Jiang and S. Wei, *Appl. Phys. Rev.*, 2017, **4**, 021304.

30 R. Jaisutti, M. Lee, J. Kim, S. Choi, T. Ha, J. Kim, H. Kim, S. K. Park and Y. Kim, *ACS Appl. Mater. Interfaces*, 2017, **9**, 8796–8804.

31 J. Zhang, X. Liu, G. Neri and N. Pinna, *Adv. Mater.*, 2016, **28**, 795–831.

32 A. Stanoiu, C. E. Simion, J. M. Calderon-Moreno, P. Osiceanu, M. Florea, V. S. Teodorescu and S. Somacescu, *J. Hazard. Mater.*, 2017, **331**, 150–160.

33 J. Chu, Q. Wang, A. Yang, J. Pan, Y. Liu, H. Yuan, M. Rong and X. Wang, *Sens. Actuators, B*, 2023, **375**, 132929.

34 D. Chen, X. Zhang, J. Tang, H. Cui and Y. Li, *Appl. Phys. A*, 2018, **124**, 194.

35 Z. Mao, J. Wang, Y. Gong, H. Yang and S. Zhang, *Micromachines*, 2018, **9**, 606.

36 C. J. Belle and U. Simon, *J. Mater. Res.*, 2013, **28**, 574–588.

37 X. Wang, D. Wang, A. Yang, N. Koratkar, J. Chu, P. Lv and M. Rong, *Phys. Chem. Chem. Phys.*, 2018, **20**, 4058–4066.

38 M. Xue, F. Li, D. Chen, Z. Yang, X. Wang and J. Ji, *Adv. Mater.*, 2016, **28**, 8265–8270.

39 Y. HE and H. JI, *Chin. J. Catal.*, 2010, **31**, 171–175.

40 D. Chen, X. Zhang, J. Tang, Z. Cui and H. Cui, *J. Hazard. Mater.*, 2019, **363**, 346–357.

41 A. Yang, D. Wang, T. Lan, J. Chu, W. Li, J. Pan, Z. Liu, X. Wang and M. Rong, *Mater. Chem. Phys.*, 2020, **240**, 122165.

42 W. Y. Chen, X. Jiang, S. Lai, D. Peroulis and L. Stanciu, *Nat. Commun.*, 2020, **11**, 1302.

43 Z. Hua, Z. Qiu, Y. Li, Y. Zeng, Y. Wu, X. Tian, M. Wang and E. Li, *Sens. Actuators, B*, 2018, **255**, 3541–3549.

44 A. A. Akande, A. G. J. Machatine, B. Masina, G. Chimowa, B. Matsoso, K. Roro, M. Duvenhage, H. Swart, J. Bandyopadhyay, S. S. Ray and B. W. Mwakikunga, *J. Phys. D: Appl. Phys.*, 2017, **51**, 015106.

45 N. P. Kondekar, M. G. Boebinger, E. V. Woods and M. T. McDowell, *ACS Appl. Mater. Interfaces*, 2017, **9**, 32394–32404.

46 X. Wang, F. Yao, P. Xu, M. Li, H. Yu and X. Li, *Nano Lett.*, 2021, **21**, 1679–1687.

47 A. Oprea, N. Bârsan and U. Weimar, *Sens. Actuators, B*, 2009, **142**, 470–493.

48 J. Chu, Q. Wang, A. Yang, J. Pan, H. Yuan, X. Wang and M. Rong, *Appl. Surf. Sci.*, 2022, **606**, 154889.

49 P. Dutta and G. Gupta, *Phys. Chem. Chem. Phys.*, 2022, **24**, 28680–28699.

50 A. Mahmood, A. Irfan and J. Wang, *Polym. Chem.*, 2022, **13**, 5961–5993.

51 A. Mahmood, A. Irfan and J. Wang, *Chin. J. Polym. Sci.*, 2022, **40**, 870–876.

52 S. Sarala, S. K. Geetha, S. Muthu and A. Irfan, *Comput. Theor. Chem.*, 2021, **1204**, 113397.

53 A. Irfan, M. Imran, R. Thomas, M. A. R. Basra, S. Ullah, A. G. Al-Sehemi and M. A. Assiri, *J. Sulfur Chem.*, 2021, **42**, 180–192.

54 J. N. Latosińska, M. Latosińska, M. A. Tomczak and W. Medycki, *J. Phys. Chem. A*, 2015, **119**, 4864–4874.

55 S. Dorotíková, K. Plevová, L. Bučinský, M. Malček, P. Herich, L. Kucková, M. Bobeničová, S. Šoralová, J. Kožíšek, M. Fronc, V. Milata and D. Dvoranová, *J. Phys. Chem. A*, 2014, **118**, 9540–9551.

56 A. Mahmood, M. I. Abdullah and M. F. Nazar, *Bull. Korean Chem. Soc.*, 2014, **35**, 1391–1396.

57 W. Li, C. Niu, J. Chu, D. Wang, P. Lv, H. Yuan, A. Yang, X. Wang, Y. Li and M. Rong, *Sens. Actuators, A*, 2019, **298**, 111590.

58 G. Kresse and D. Joubert, *Phys. Rev. B: Condens. Matter Mater. Phys.*, 1999, **59**, 1758–1775.

59 J. P. Perdew, K. Burke and M. Ernzerhof, *Phys. Rev. Lett.*, 1996, **77**, 3865–3868.

60 P. E. Blöchl, *Phys. Rev. B: Condens. Matter Mater. Phys.*, 1994, **50**, 17953–17979.

61 S. Grimme, *J. Comput. Chem.*, 2006, **27**, 1787–1799.

62 T. Bucko, S. Lebegue, J. G. Angyan and J. Hafner, *J. Chem. Phys.*, 2014, **141**, 034114.

63 V. Sharma, B. Roondhe, S. Saxena and A. Shukla, *Int. J. Hydrogen Energy*, 2022, **47**, 41748–41758.

64 A. I. Martinez, *J. Nano Res.*, 2009, **5**, 113–119.

65 J. Singh, R. Thareja, P. Malik and R. Kakkar, *J. Nanopart. Res.*, 2022, **24**, 33.

66 B. K. Sahu, G. Kaur and A. Das, *ACS Appl. Mater. Interfaces*, 2020, **12**, 49227–49236.

67 A. Mahmood, G. Shi, Z. Wang, Z. Rao, W. Xiao, X. Xie and J. Sun, *J. Hazard. Mater.*, 2021, **401**, 123402.

68 S. Keshtkar, A. Rashidi, M. Kooti, M. Askarieh, S. Pourhashem, E. Ghasemy and N. Izadi, *Talanta*, 2018, **188**, 531–539.

69 Y. Qin and Z. Ye, *Sens. Actuators, B*, 2016, **222**, 499–507.

70 M. Srivastava and A. Srivastava, *Chem. Phys. Lett.*, 2019, **729**, 17–23.

71 J. Shang, G. Li, R. Singh, P. Xiao, D. Danaci, J. Z. Liu and P. A. Webley, *J. Chem. Phys.*, 2014, **140**, 84705.

72 X. Wang, T. Wang, G. Si, Y. Li, S. Zhang, X. Deng and X. Xu, *Sens. Actuators, B*, 2020, **302**, 127165.

73 A. E. Reed, R. B. Weinstock and F. Weinhold, *J. Chem. Phys.*, 1985, **83**, 735–746.

74 S. Saha, R. K. Roy and P. W. Ayers, *Int. J. Quantum Chem.*, 2009, **109**, 1790–1806.

75 Z. Zhen, Z. Jijun, C. Yongsheng, V. Paul and S. Ragué, *Nanotechnology*, 2007, **18**, 424023.

76 X. Zhang, Y. Gui, H. Xiao and Y. Zhang, *Appl. Surf. Sci.*, 2016, **379**, 47–54.

77 A. Hosseinian, Z. Asadi, L. Edjlali, A. Bekhradnia and E. Vessally, *Comput. Theor. Chem.*, 2017, **1106**, 36–42.

78 M. Liu, J. Ji, P. Song, M. Liu and Q. Wang, *Sens. Actuators, B*, 2021, **349**, 130782.

79 A. Yang, D. Wang, X. Wang, J. Chu, P. Lv, Y. Liu and M. Rong, *IEEE Electron Device Lett.*, 2017, **38**, 963–966.

80 Z. Xu, Z. Shi, M. Wang, R. Song, X. Zhang, G. Liu and G. Qiao, *Sens. Actuators, A*, 2021, **328**, 112766.

81 D. Wang, A. Yang, T. Lan, C. Fan, J. Pan, Z. Liu, J. Chu, H. Yuan, X. Wang, M. Rong and N. Koratkar, *J. Mater. Chem. A*, 2019, **7**, 26326–26333.

82 D. Wang, J. Pan, T. Lan, J. Chu, C. Fan, H. Yuan, Y. Wu, A. Yang, X. Wang and M. Rong, *ACS Appl. Nano Mater.*, 2020, **3**, 7587–7594.

83 M. S. Khan, V. Ranjan and A. Srivastava, *2015 IEEE Int. Symp. Nanoelectron. Inform. Syst.*, 2015, pp. 248–251.

84 A. Yang, J. Pan, D. Wang, T. Lan, Z. Liu, H. Yuan, J. Chu, X. Wang and M. Rong, *Appl. Surf. Sci.*, 2020, **523**, 146403.

85 X. Wang, D. Wang, Z. Liu, T. Lan, A. Yang, J. Pan, J. Chu, H. Yuan and M. Rong, *IEEE Electron. Device Lett.*, 2020, **41**, 1408–1411.

86 Y. Su, W. Li, X. Cheng, Y. Zhou, S. Yang, X. Zhang, C. Chen, T. Yang, H. Pan and G. Xie, *Nat. Commun.*, 2022, **13**, 4867.

87 H. Tang, Y. Li, R. Sokolovskij, L. Sacco, H. Zheng, H. Ye, H. Yu, X. Fan, H. Tian and T. Ren, *ACS Appl. Mater. Interfaces*, 2019, **11**, 40850–40859.

88 J. Huang, J. Chu, Z. Wang, J. Zhang, A. Yang, X. Li, C. Gao, H. Huang, X. Wang, Y. Cheng and M. Rong, *ChemNanoMat*, 2019, **5**, 1123–1130.

89 D. Wang, T. Lan, J. Pan, Z. Liu, A. Yang, M. Yang, J. Chu, H. Yuan, X. Wang, Y. Li and M. Rong, *Sens. Actuators, A*, 2020, **311**, 112049.

90 C. Niu, T. Lan, D. Wang, J. Pan, J. Chu, C. Wang, H. Yuan, A. Yang, X. Wang and M. Rong, *Appl. Surf. Sci.*, 2020, **520**, 146257.

91 D. Wang, T. Lan, A. Yang, J. Pan, J. Chu, H. Yuan, Y. Li, X. Wang and M. Rong, *IEEE Sens. J.*, 2020, **20**, 8997–9003.

92 H. Cui, X. Zhang, G. Zhang and J. Tang, *Appl. Surf. Sci.*, 2019, **470**, 1035–1042.

93 I. Karaduman, E. Er, H. Çelikkan, N. Erk and S. Acar, *J. Alloys Compd.*, 2017, **722**, 569–578.

94 D. Wang, X. Wang, A. Yang, P. Lv, J. Chu, Y. Liu, M. Rong and C. Wang, *Mater. Chem. Phys.*, 2018, **212**, 453–460.

95 M. Brandbyge, J. L. Mozos, P. Ordejon, J. Taylor and K. Stokbro, *Phys. Rev. B: Condens. Matter Mater. Phys.*, 2002, **65**, 5401.

96 J. Q. You, C. H. Lam and H. Z. Zheng, *Phys. Rev. B: Condens. Matter Mater. Phys.*, 2000, **62**, 1978–1983.

97 R. Vasumathi, A. Thayumanavan and S. Sriram, *J. Electron. Mater.*, 2017, **46**, 4140–4146.

98 S. Sriram, V. Nagarajan and R. Chandiramouli, *Chem. Phys. Lett.*, 2015, **636**, 51–57.

99 R. Bhuvaneswari, J. P. Maria, V. Nagarajan and R. Chandiramouli, *Chem. Phys. Lett.*, 2020, **747**, 137353.

100 N. Yamazoe, K. Suematsu and K. Shimanoe, *Sens. Actuators, B*, 2012, **163**, 128–135.

101 F. Montejo-Alvaro, J. Oliva, M. Herrera-Trejo, H. M. Hdz-García and A. I. Mtz-Enriquez, *Theor. Chem. Acc.*, 2019, **138**, 37.

102 M. A. H. Khan, B. Thomson, A. Motayed, Q. Li and M. V. Rao, *IEEE Sens. J.*, 2020, **20**, 7138–7147.

103 D. Wang, X. Wang, A. Yang, J. Chu, P. Lv, Y. Liu and M. Rong, *IEEE Electron. Device Lett.*, 2018, **39**, 292–295.

104 X. H. Wang, D. W. Wang, A. J. Yang, N. Koratkar, J. F. Chu, P. L. Lv and M. Z. Rong, *Phys. Chem. Chem. Phys.*, 2018, **20**, 4058–4066.

105 F. Behmagham, E. Vessally, B. Massoumi, A. Hosseinian and L. Edjlali, *Superlattices Microstruct.*, 2016, **100**, 350–357.

106 S. Yan, X. Liang, H. Song, S. Ma and Y. Lu, *Ceram. Int.*, 2018, **44**, 358–363.

107 M. S. Choi, H. G. Na, J. H. Bang, A. Mirzaei, S. Han, H. Y. Lee, S. S. Kim, H. W. Kim and C. Jin, *Sens. Actuators, B*, 2021, **326**, 128801.

108 H. Liu, M. Li, O. Voznyy, L. Hu, Q. Fu, D. Zhou, Z. Xia, E. H. Sargent and J. Tang, *Adv. Mater.*, 2014, **26**, 2718–2724.

109 S. Choi, M. Bonyani, G. Sun, J. K. Lee, S. K. Hyun and C. Lee, *Appl. Surf. Sci.*, 2018, **432**, 241–249.

110 J. Tan, M. Dun, L. Li, J. Zhao, W. Tan, Z. Lin and X. Huang, *Sens. Actuators, B*, 2017, **249**, 44–52.

111 B. Zhang, M. Li, Z. Song, H. Kan, H. Yu, Q. Liu, G. Zhang and H. Liu, *Sens. Actuators, B*, 2017, **249**, 558–563.

112 L. Guo, F. Chen, N. Xie, X. Kou, C. Wang, Y. Sun, F. Liu, X. Liang, Y. Gao, X. Yan, T. Zhang and G. Lu, *Sens. Actuators, B*, 2018, **272**, 185–194.

113 W. Koo, S. Choi, S. Kim, J. Jang, H. L. Tuller and I. Kim, *J. Am. Chem. Soc.*, 2016, **138**, 13431–13437.

114 T. He, W. Liu, T. Lv, M. Ma, Z. Liu, A. Vasiliev and X. Li, *Sens. Actuators, B*, 2021, **329**, 129275.

115 D. Gu, X. Li, Y. Zhao and J. Wang, *Sens. Actuators, B*, 2017, **244**, 67–76.

116 Z. Song, Z. Wei, B. Wang, Z. Luo, S. Xu, W. Zhang, H. Yu, M. Li, Z. Huang, J. Zang, F. Yi and H. Liu, *Chem. Mater.*, 2016, **28**, 1205–1212.

117 J. Chu, X. Wang, D. Wang, A. Yang, P. Lv, Y. Wu, M. Rong and L. Gao, *Carbon*, 2018, **135**, 95–103.

118 Z. Hua, Y. Li, Y. Zeng and Y. Wu, *Sens. Actuators, B*, 2018, **255**, 1911–1919.

119 P. K. Clifford and D. T. Tuma, *Sens. Actuators*, 1983, **3**, 233–254.

120 M. Akiyama, J. Tamaki, N. Miura and N. Yamazoe, *Chem. Lett.*, 1991, 1611–1614.

121 D. D. Vuong, G. Sakai, K. Shimanoe and N. Yamazoe, *Sens. Actuators, B*, 2004, **103**, 386–391.

122 P. M. Desimone, F. Schipani, R. Procaccini, D. A. Mirabella and C. M. Aldao, *Sens. Actuators, B*, 2022, **370**, 132387.

123 N. Barsan, J. Rebholz and U. Weimar, *Sens. Actuators, B*, 2015, **207**, 455–459.

124 S. Maeng, S. Kim, D. Lee, S. Moon, K. Kim and A. Maiti, *ACS Appl. Mater. Interfaces*, 2014, **6**, 357–363.

125 A. A. Akande, E. C. Linganiso, B. P. Dhonge, K. E. Rammutla, A. Machatine, L. Prinsloo, H. Kunert and B. W. Mwakikunga, *Mater. Chem. Phys.*, 2015, **151**, 206–214.

126 J. Z. Ou, W. Ge, B. Carey, T. Daeneke, A. Rotbart, W. Shan, Y. Wang, Z. Fu, A. F. Chrimes, W. Wlodarski, S. P. Russo, Y. X. Li and K. Kalantar-zadeh, *ACS Nano*, 2015, **9**, 10313–10323.

127 K. J. Dunst, K. Trzciński, B. Scheibe, M. Sawczak and P. Jasiński, *Sens. Actuators, B*, 2018, **260**, 1025–1033.

128 D. E. Starr, Z. Liu, M. Haevecker, A. Knop-Gericke and H. Bluhm, *Chem. Soc. Rev.*, 2013, **42**, 5833–5857.

129 V. I. Sysoev, A. V. Okotrub, A. V. Gusel'Nikov, D. A. Smirnov and L. G. Bulusheva, *Phys. Status Solidi B*, 2018, **255**, 1700267.

130 S. Yamamoto, H. Bluhm, K. Andersson, G. Ketteler, H. Ogasawara, M. Salmeron and A. Nilsson, *J. Phys.: Condens. Matter*, 2008, **20**, 184025.

131 H. W. Cheng, S. Wang, G. Chen, Z. Liu, D. Caracciolo, M. Madiou, S. Shan, J. Zhang, H. He, R. Che and C. J. Zhong, *Adv. Energy Mater.*, 2022, **12**, 2202097.

132 X. Wang, M. Li, P. Xu, Y. Chen, H. Yu and X. Li, *Nano Lett.*, 2022, **22**, 3157–3164.

133 A. D'Amico, C. Di Natale, R. Paolesse, A. Mantini, C. Goletti, F. Davide and G. Filosofi, *Sens. Actuators, B*, 2000, **70**, 254–262.

134 R. Pearce, J. Eriksson, T. Iakimov, L. Hultman, A. Lloyd Spetz and R. Yakimova, *ACS Nano*, 2013, **7**, 4647–4656.

135 C. E. Simion, F. Schipani, A. Papadogianni, A. Stanoiu, M. Budde, A. Oprea, U. Weimar, O. Bierwagen and N. Barsan, *ACS Sens.*, 2019, **4**, 2420–2428.

136 A. Stanoiu, S. Somacescu, J. M. Calderon-Moreno, V. S. Teodorescu, O. G. Florea, A. Sackmann and C. E. Simion, *Sens. Actuators, B*, 2016, **231**, 166–174.

137 S. H. Soytas, J. E. Puskas and K. Kulbaba, *J. Polym. Sci., Polym. Chem. Ed.*, 2008, **46**, 3611–3618.

138 K. L. A. Chan and S. G. Kazarian, *Chem. Soc. Rev.*, 2016, **45**, 1850–1864.

139 T. Shinkai, K. Masumoto, M. Iwai, Y. Inomata and T. Kida, *Sensors*, 2022, **22**, 6277.

140 H. Kim, A. Haensch, I. Kim, N. Barsan, U. Weimar and J. Lee, *Adv. Funct. Mater.*, 2011, **21**, 4456–4463.

141 L. Zhang, L. Li, Y. Cao, X. Yao, C. Ge, F. Gao, Y. Deng, C. Tang and L. Dong, *Appl. Catal., B*, 2015, **165**, 589–598.

142 K. Grossmann, R. G. Pavelko, N. Barsan and U. Weimar, *Sens. Actuators, B*, 2012, **166–167**, 787–793.

143 Z. Zhang, K. Huang, F. Yuan and C. Xie, *Appl. Surf. Sci.*, 2014, **300**, 98–103.

144 J. Song, K. Huang and N. Wang, *J. Mater. Res.*, 2016, **31**, 2035–2045.

145 S. Luo, J. Liu and Z. Wu, *J. Phys. Chem. C*, 2019, **123**, 11772–11780.

146 G. Chimowa, B. Matsoso, N. J. Coville, S. S. Ray, E. Flahaut, T. Hungria, L. Datas and B. W. Mwakikunga, *Phys. Status Solidi A*, 2017, **214**, 1600930.

147 J. Zhou, S. Blomberg, J. Gustafson, E. Lundgren and J. Zetterberg, *Catalysts*, 2017, **7**, 29.

148 L. Zou, P. Cao, Y. Lei, D. Zakharov, X. Sun, S. D. House, L. Luo, J. Li, Y. Yang, Q. Yin, X. Chen, C. Li, H. Qin, E. A. Stach, J. C. Yang, G. Wang and G. Zhou, *Nat. Commun.*, 2020, **11**, 3934.

149 K. Grossmann, N. Barsan and U. Weimar, *Procedia Eng.*, 2010, **5**, 119–122.